

Supplementary Information

Physically Separate Yet Perceptually Fused: Interdigitated Electrode-Architected Electrochromic Film for Decoupled Modulation of Visible and Infrared Camouflage

Hengzhi Zhang¹, Junyu Yuan^{1,2}, Yulin Liu¹, Yijia Cui¹, Pingfan Chen¹,

Rongzong Zheng^{1,3,}, Chunyang Jia^{1,*}*

¹National Key Laboratory of Electronic Thin Films and Integrated Devices, National Engineering Research Center of Electromagnetic Radiation Control Materials, School of Integrated Circuit Science and Engineering, University of Electronic Science and Technology of China, Chengdu 611731, P. R. China.

²Shenzhen Institute for Advanced Study, University of Electronic Science and Technology of China, 518110 Shenzhen, China.

³College of Materials and Metallurgy, Guizhou University, Guiyang 550025, P. R. China.

* Corresponding author: E-mail: cyjia@uestc.edu.cn

Experimental Section

Materials

Ferric chloride、37 % hydrochloric acid、98 % sulfuric acid、hydrogen peroxide、ethanol、acetone、propylene carbonate purchased from Chengdu Kelon Chemical Co. Aniline、titanium oxide、potassium ferricyanide、potassium chloride、sodium tungstate dihydrate、lithium perchlorate、polymethyl methacrylate purchased from Shanghai Aladdin Biochemical Technology Co. The chemicals are used directly without additional purification.

Fabrication of Electrochromic Layers

ITO or Au/Nylon 66 electrodes served as the growth substrates for the ECLs. PB, PANI, and WO₃ are electrochemically deposited using a three-electrode configuration comprising a Pt counter electrode and an Ag/AgCl reference electrode. PB is electrodeposited from a precursor solution containing 100 mL deionized water, 2 mL 37 % hydrochloric acid, 0.745 g potassium chloride, 0.13 g ferric chloride, and 0.165 g potassium ferricyanide at a constant current density of 25 $\mu\text{A cm}^{-2}$. PANI is deposited using a two-step potentiostatic method from a solution consisting of 100 mL deionized water, 5 mL 98 % sulfuric acid, and 1 mL aniline, with step 1 at 0.8 V for 300 s followed by step 2 at 0.6 V for 600 s. WO₃ is deposited from a precursor solution composed of 100 mL deionized water, 0.26 mL hydrogen peroxide, 0.4 mL 98 % sulfuric acid, and 0.41 g sodium tungstate dihydrate at a constant potential of -0.7 V. After ECL deposition, all samples are thoroughly rinsed with deionized water and dried in an oven at 60 °C for 12 h. The TiO₂ is spin-coated onto the electrode surface at 1800 rpm with a dropping rate of 0.1 mL s⁻¹ (total volume: 0.6-0.8 mL). The coated samples are then dried in an oven at 100 °C for 1 h, followed by annealing on a hotplate at a heating rate of 5 °C min⁻¹ to 450 °C and maintaining this temperature for 1 h.

Assembly of Dual-band Decoupled Electrochromic Film

The interdigitated Au/Nylon 66 electrode is fabricated via CO₂ laser ablation at 30 W, selectively removing the Au layer on the Nylon 66 substrate to form insulated serpentine patterns. The etched electrode exhibits electrical isolation between complementary finger regions, thereby enabling the original Au/Nylon 66 electrode to be electrically and spatially partitioned into independent Vis and IR modulation regions by the interdigitated electrode stripes. Meanwhile, the

interdigitated electrode stripes are electrically connected to the continuous conductive regions on both sides, providing the necessary conditions for the growth of EC materials. The interdigitated electrode is sequentially immersed in PANI and PB precursor solutions, with PB and PANI selectively grown in the Vis and IR modulation regions, respectively, yielding D-ECL. Thereafter, the D-ECL is integrated with an ion-storage layer (ISL) via a gel-state electrolyte to fabricate the D-ECF with multiple tuning freedoms.

Characterization

ECL morphology is characterized via SEM (ZEISS Gemini 300) and AFM (Bruker Dimension ICON). Elemental valence states of EC materials are determined using XPS (Thermo Scientific K-Alpha). Their phase composition and structure are analyzed by FT-IR (Spectrum GX, Perkin-Elmer) and XRD (D8 Advance, Bruker). Electrochemical deposition and property tests are performed on an electrochemical workstation (CHI660E, Shanghai ChenHua Technologies). Vis and thermal IR reflectance modulation of D-ECF is measured via a UV-Vis-NIR spectrophotometer (Lambda 900, Perkin-Elmer) and reflectance-mode FT-IR spectrometer (Frontier, Perkin-Elmer). LWIR imaging is conducted using a MAG 32 system (Shanghai Magnity Technologies).

Methods

M. S1 The similarity between PB-ECL and PANI-ECL is assessed using the correlation coefficient (S1).

$$S_{ij} = \frac{\sum_{i=1}^m (X_{ik} - \bar{X}_i)(X_{jk} - \bar{X}_j)}{\sqrt{\sum_{k=1}^m (X_{ik} - \bar{X}_i)^2 \sum_{k=1}^m (X_{jk} - \bar{X}_j)^2}} \quad (S1)$$

Here, X_{ik} and X_{jk} represent the spectral values of PB-ECL and PANI-ECL at spectral point k , respectively. \bar{X}_i and \bar{X}_j represent the average value of reflectivity spectra i and j , respectively, and spectral similarity coefficient S_{ij} indicates the similarity of two spectral curves. The higher the spectral similarity, the closer the spectral similarity

coefficient to 1. The vector cosine angle is also used to assess the similarity between PB-ECL and PANI-ECL (S2).

$$SAM(x_i, x_j) = \cos^{-1} \frac{\sum_{k=1}^m X_{ik} X_{jk}}{\sqrt{\sum_{k=1}^m X_{ik}^2} \sqrt{\sum_{k=1}^m X_{jk}^2}} \quad (S2)$$

The higher the similarity of the spectral curves, the closer the similarity coefficient is to 0.

M. S2 The CIE standard colorimetric system is calculated from spectral reflectance $R(\lambda)$ (S3, S4, and S5).

$$X = K \sum_{\lambda} [R(\lambda) S(\lambda) x(\lambda) \Delta\lambda] \quad (S3)$$

$$Y = K \sum_{\lambda} [R(\lambda) S(\lambda) y(\lambda) \Delta\lambda] \quad (S4)$$

$$Z = K \sum_{\lambda} [R(\lambda) S(\lambda) z(\lambda) \Delta\lambda] \quad (S5)$$

$K = 100 / \sum_{\lambda} S(\lambda) y(\lambda) \Delta\lambda$, where $S(\lambda)$ is the spectral power distribution of the standard illuminant, $x(\lambda) y(\lambda) z(\lambda)$ is the chromaticity matching function, and $\Delta\lambda$ is the spectral sampling interval.

Subsequently, the $L^*a^*b^*$ color coordinates are calculated using the $X Y Z$ system.

When $Y/Y_n > 0.008856$ (S6), $Y/Y_n \leq 0.008856$ (S7).

$$L^* = \left(116 \frac{Y}{Y_n}^{1/3} - 16 \right) \quad a^* = 500 \left(\frac{X}{X_n}^{1/3} - \frac{Y}{Y_n}^{1/3} \right) \quad b^* = 200 \left(\frac{X}{X_n}^{1/3} - \frac{Y}{Y_n}^{1/3} \right) \quad (S6)$$

$$L^* = 903.3 \frac{Y}{Y_n} \quad a^* = 3893.5 \left(\frac{X}{X_n} - \frac{Y}{Y_n} \right) \quad b^* = 1557.4 \left(\frac{Y}{Y_n} - \frac{Z}{Z_n} \right) \quad (S7)$$

M. S3 The color difference ΔE_{76} in the CIE1976 $L^*a^*b^*$ color coordinate system is calculated using the following formula (S8).

$$\Delta E_{76} = [(\Delta L^*)^2 + (\Delta a^*)^2 + (\Delta b^*)^2]^{\frac{1}{2}} \quad (\text{S8})$$

M. S4 The Randles-Sevcik equation is used to quantify the ion diffusion rates of PB-ECL and PANI-ECL (S9).

$$I_p = 0.446nFAC \left(\frac{nFvD}{RT} \right)^{1/2} \quad (\text{S9})$$

I_p is the peak current, n is the number of electrons transferred during the redox process, F is the Faraday constant, A is the active area, C is the concentration of Li^+ in the electrolyte, D is the diffusion coefficient, v is the scan rate, R is the gas constant, and T is the temperature (298.15 K).

M. S5 PANI-ECL's average emissivity ($a-\varepsilon$) regulation is calculated via wavelength integration of monochromatic emissivity across bands (S10 and S11).

$$B(\lambda) = \frac{2\pi hc^2}{\lambda^5} \times \frac{1}{e^{\left(\frac{hc}{\lambda\sigma T}\right)} - 1} \quad (\text{S10})$$

$$a - \varepsilon = \frac{\int_{\lambda_{min}}^{\lambda_{max}} (1 - R(\lambda)) \times B(\lambda) d\lambda}{\int_{\lambda_{min}}^{\lambda_{max}} B(\lambda) d\lambda} \quad (\text{S11})$$

In this context, σ is the Boltzmann constant, Planck's constant is denoted by h , the speed of light is represented as c , the wavelength is defined as λ , and the temperature is denoted as T . At wavelength λ , the spectral blackbody radiance and hemispherical reflectance are quantitatively described by $B(\lambda)$ and $R(\lambda)$, respectively, where λ denotes

the specific wavelength under consideration.

M. S6 Since monochromatic emissivity at wavelength λ equals the ratio of actual emissive power to blackbody emissive power at the same temperature, PANI-ECL's monochromatic emissive power at λ can be calculated using blackbody emissive power at λ (S12).

$$\varepsilon_{\lambda} = \frac{E_{\lambda}}{E_{b\lambda=}} \quad (\text{S12})$$

M. S7 Rayleigh criterion evaluates the camouflage effectiveness of pixelated D-ECF (S13).

$$d \cdot \theta \geq \frac{l \cdot 2.54}{\sqrt{w^2 h^2}} \quad (\text{S13})$$

Here, d represents the resolvable distance, l denotes the diagonal dimension of the D-ECF, and w and h denote the pixel counts of horizontal/vertical interdigitated electrode stripes, respectively. Higher pixel density corresponds to a shorter distinguishable distance between pixels.

M. S8 The apparent temperature in thermal imaging can be estimated by Equation S14.

$$I_{det} = \epsilon \cdot \sigma T_{obj}^4 + (1 - \epsilon) \cdot \sigma T_{env}^4 \quad (\text{S14})$$

I_{det} refers to the total radiant intensity received by the detector; ϵ is the surface emissivity of the material ($0 \leq \epsilon \leq 1$), σ is the Stefan-Boltzmann constant, T_{obj} is the true temperature of the object, and T_{env} is the ambient temperature (e.g., walls, human bodies, etc.). When the ambient temperature is higher than the object temperature, the dominance of reflected ambient radiation leads to an overestimation of the apparent temperature.

Supporting Figures and Tables

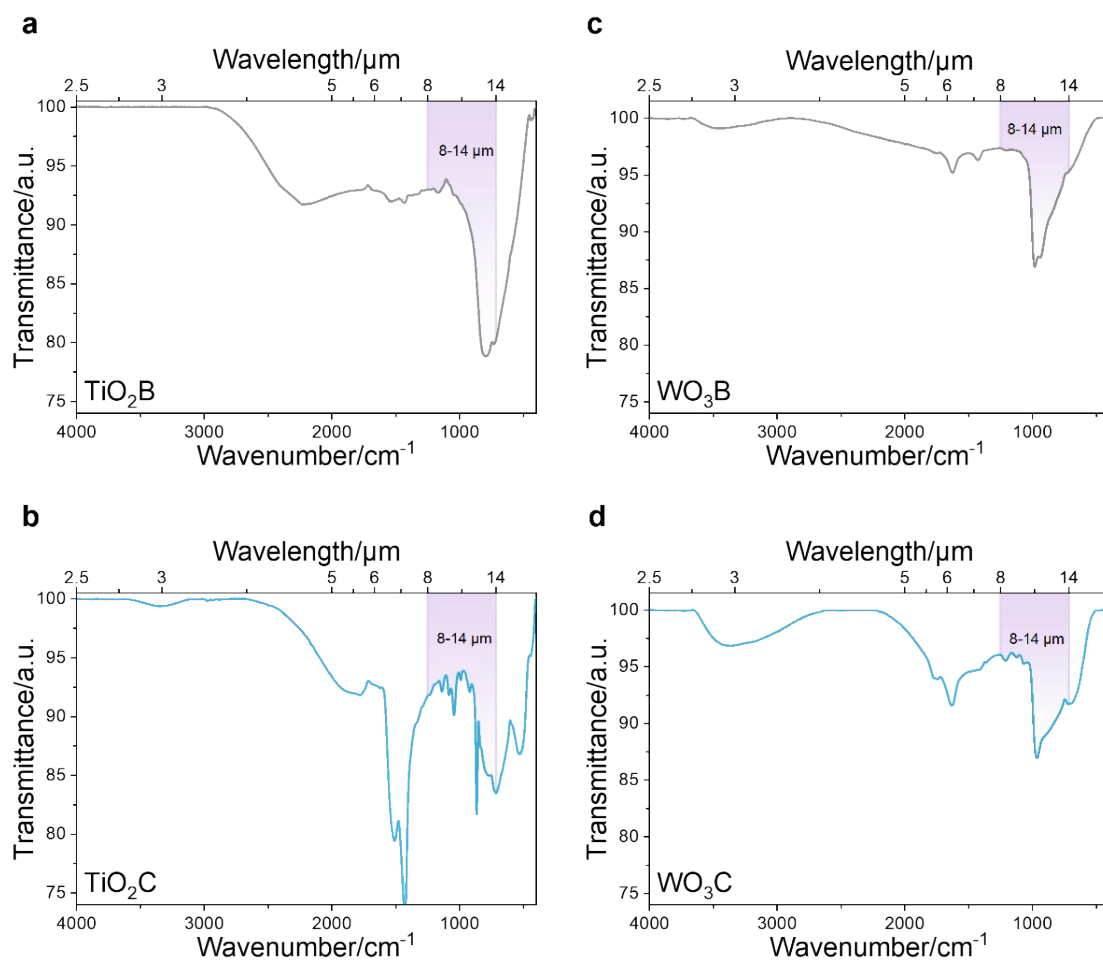


Figure. S1 WO₃ and TiO₂ are deposited on ITO surfaces via electrodeposition and spin-coating, respectively, and tested. FT-IR transmittance spectra of TiO₂ in the (a) bleached state and (b) colored state, and FT-IR transmittance spectra of WO₃ in the (c) bleached state and (d) colored state.

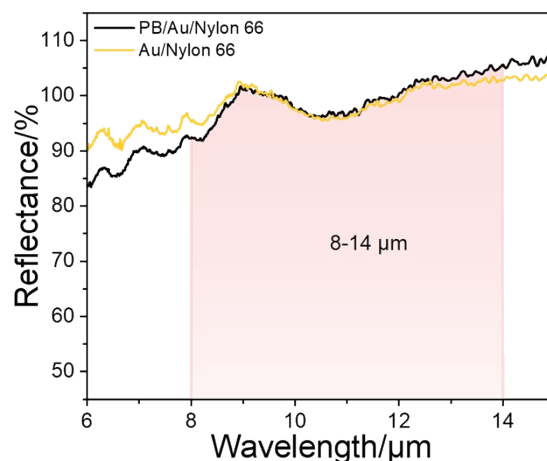


Figure. S2 Mid-to-far IR reflectance spectra of Au/Nylon 66 before and after PB deposition

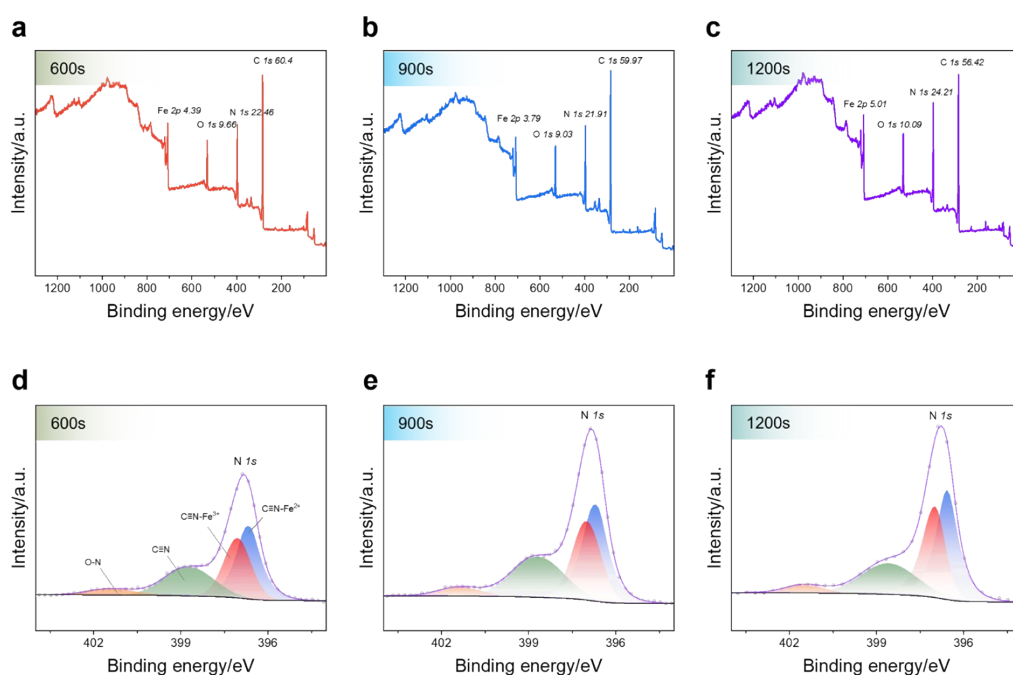


Figure. S3 The survey XPS spectra of PB-ECL with different deposition times of (a) 600s, (b) 900s, and (c) 1200s. The high-resolution N $1s$ spectra of PB-ECL with different deposition times of (d) 600s, (e) 900s, and (f) 1200s.

The peaks centered at 396.7 eV and 397.1 eV are assigned to C \equiv N-Fe $^{2+}$ and C \equiv N-Fe $^{3+}$ bonds, respectively, and their ratio is approximately 5:4.

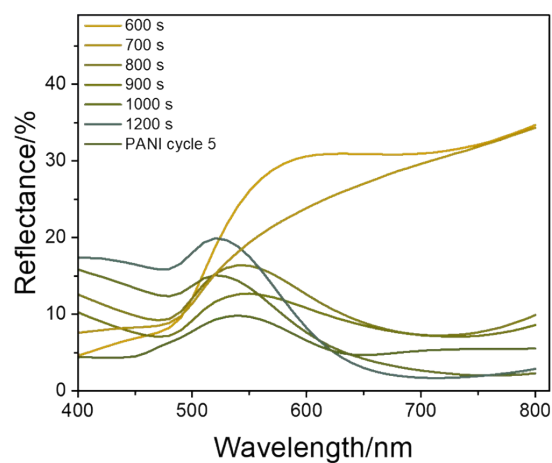


Figure. S4 Matching of spectral reflectance in the Vis range between PANI-ECL and PB-ECL with different deposition times.

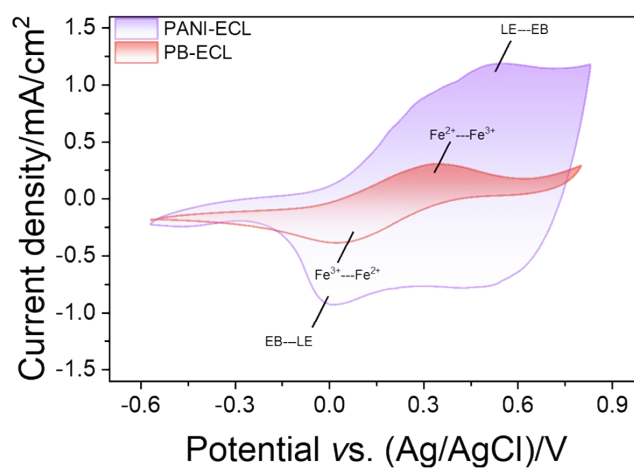


Figure S5. CV curves of PANI-ECL and PB-ECL in the potential range of -0.6 V to 0.8 V at a scan rate of 15 mV s⁻¹.

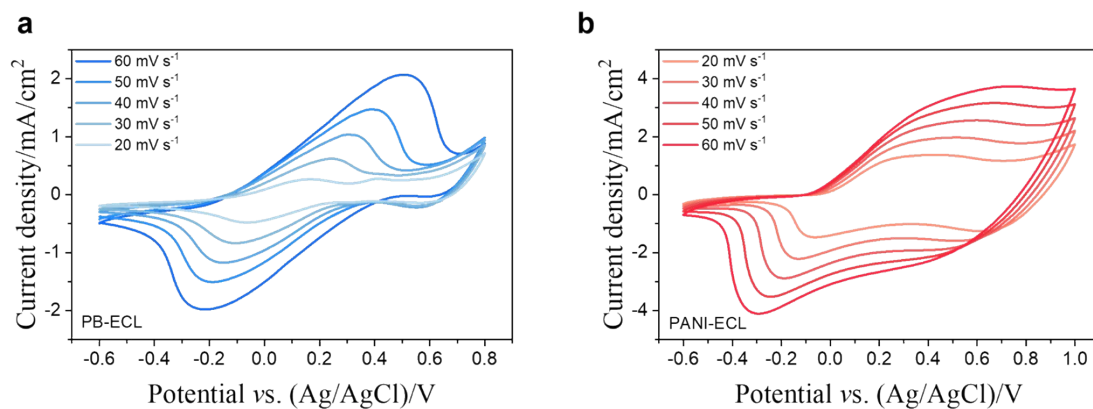


Figure S6. CV curve variations of (a) PB-ECL and (b) PANI-ECL at scan rates ranging from 20 to 60 mV s^{-1} .

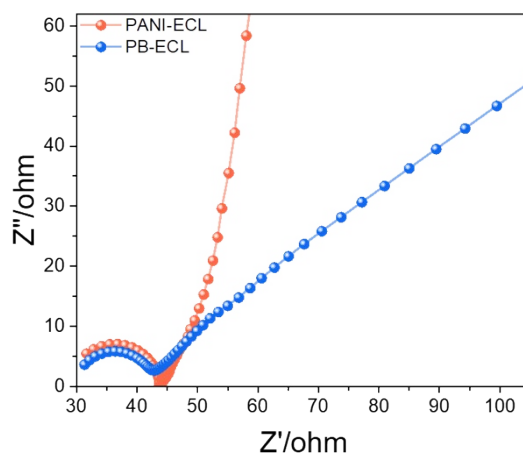


Figure S7. Electrochemical impedance spectroscopy-Nyquist curve.

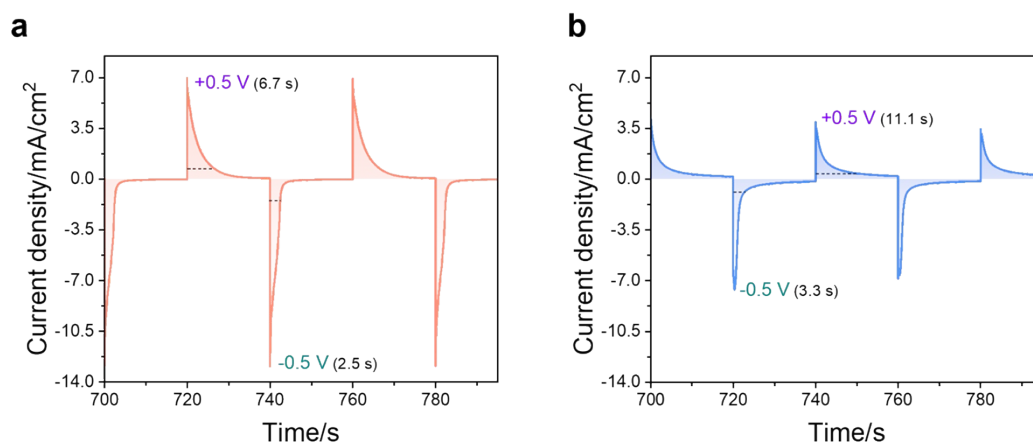


Figure S8. Alternating potential response for (a) PANI-ECL versus (b) PB-ECL.

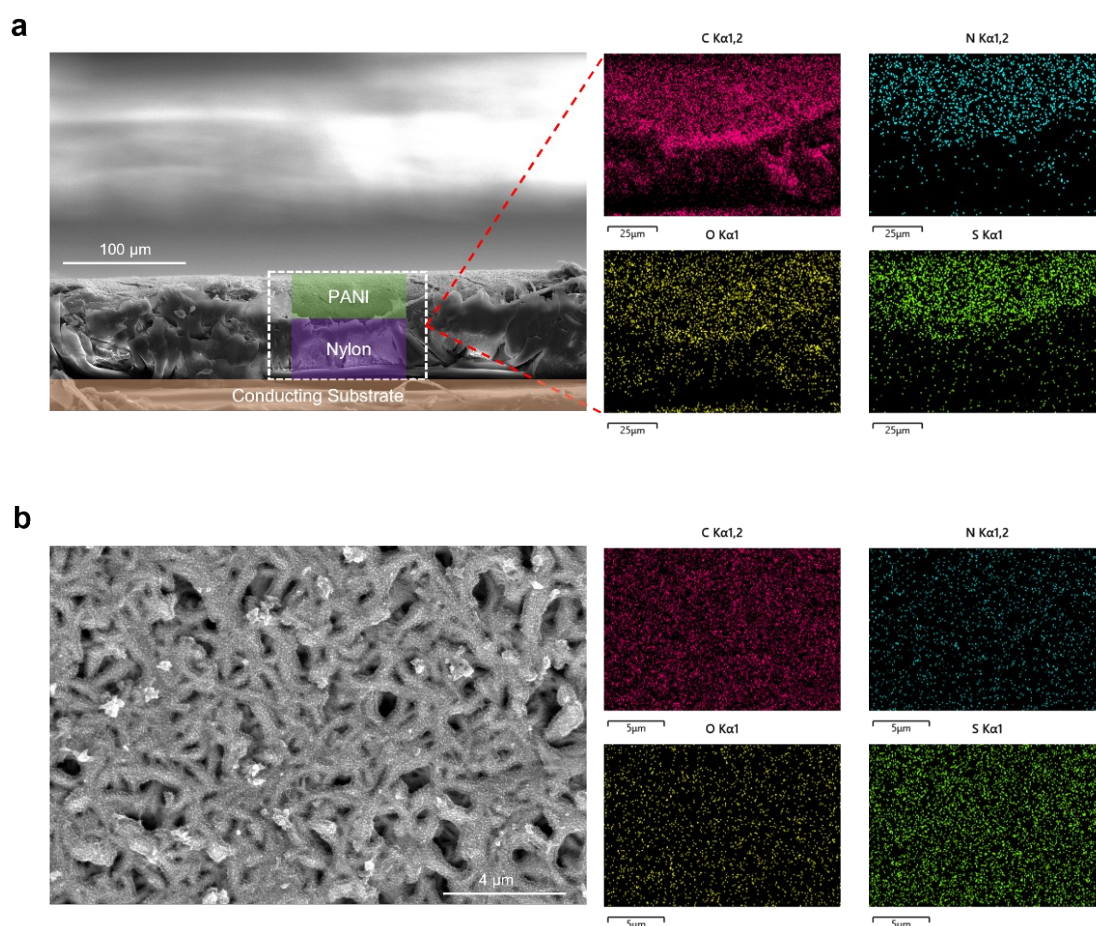


Figure S9. (a) Cross-sectional SEM imaging and EDS-mapping elemental distribution of PANI-ECL. (b) Surface SEM imaging and EDS-mapping elemental distribution of PANI-ECL.

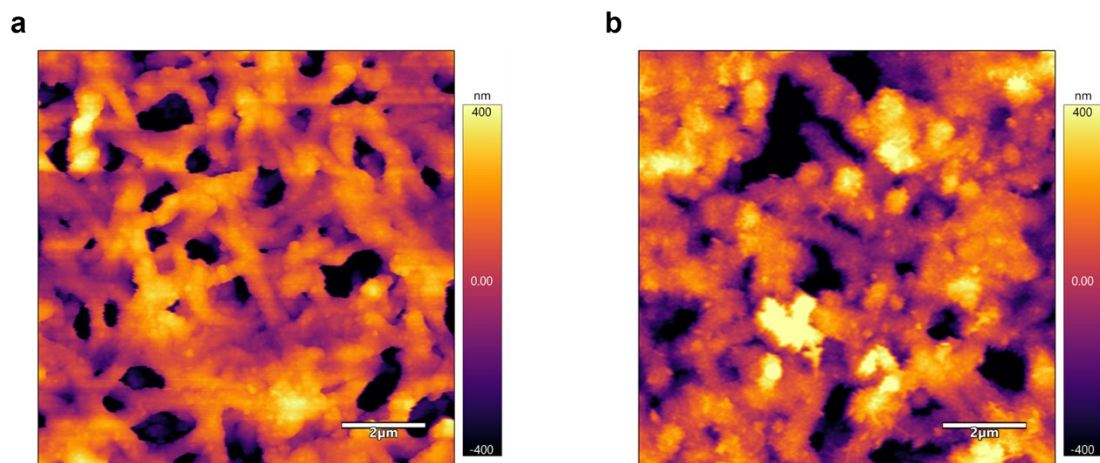


Figure S10. 2D AFM images of (a) PB-ECL and (b) PANI-ECL.

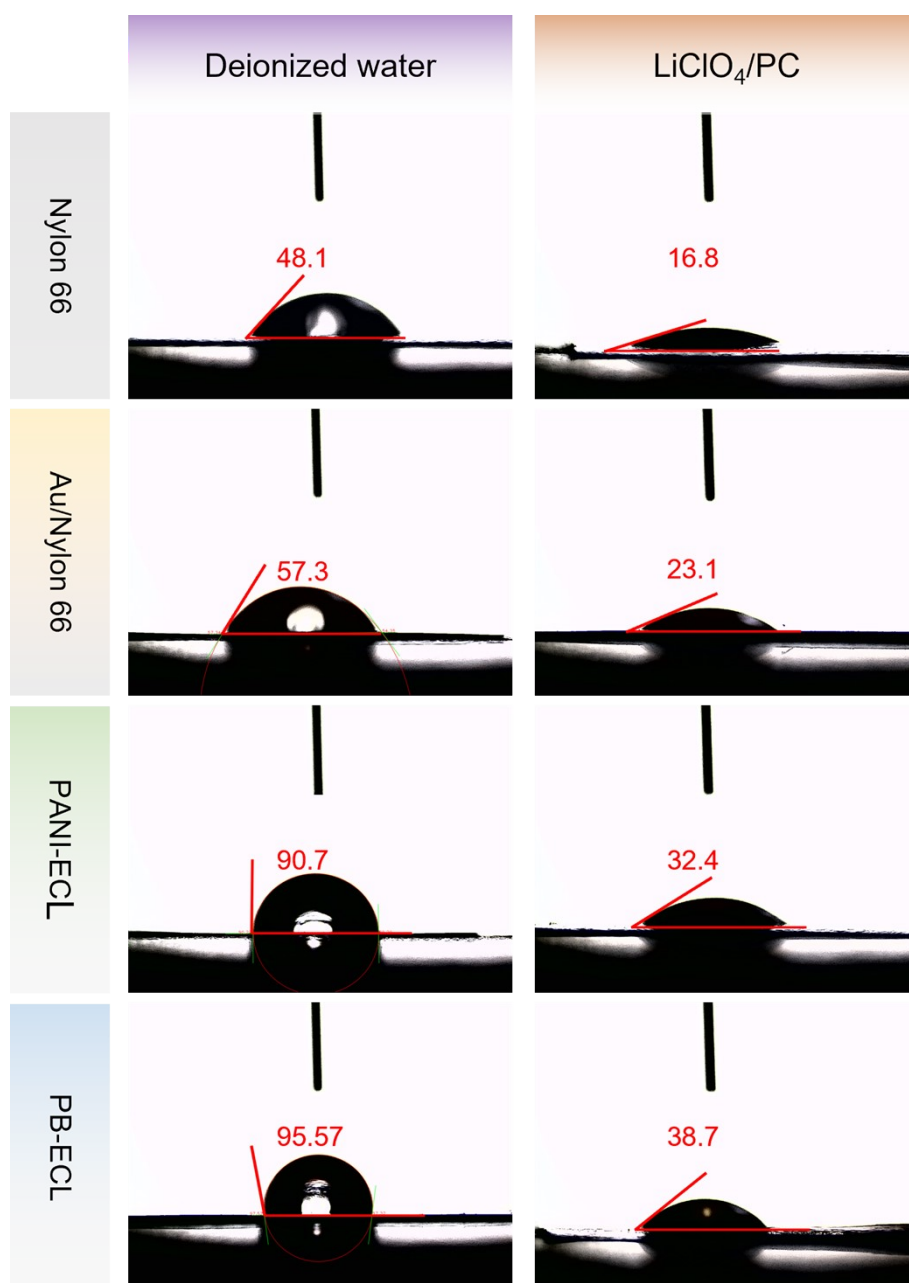


Figure S11. Contact angles of Nylon 66, Au/Nylon 66 substrates, PANI-ECL, and PB-ECL (deionized water and lithium perchlorate electrolyte)

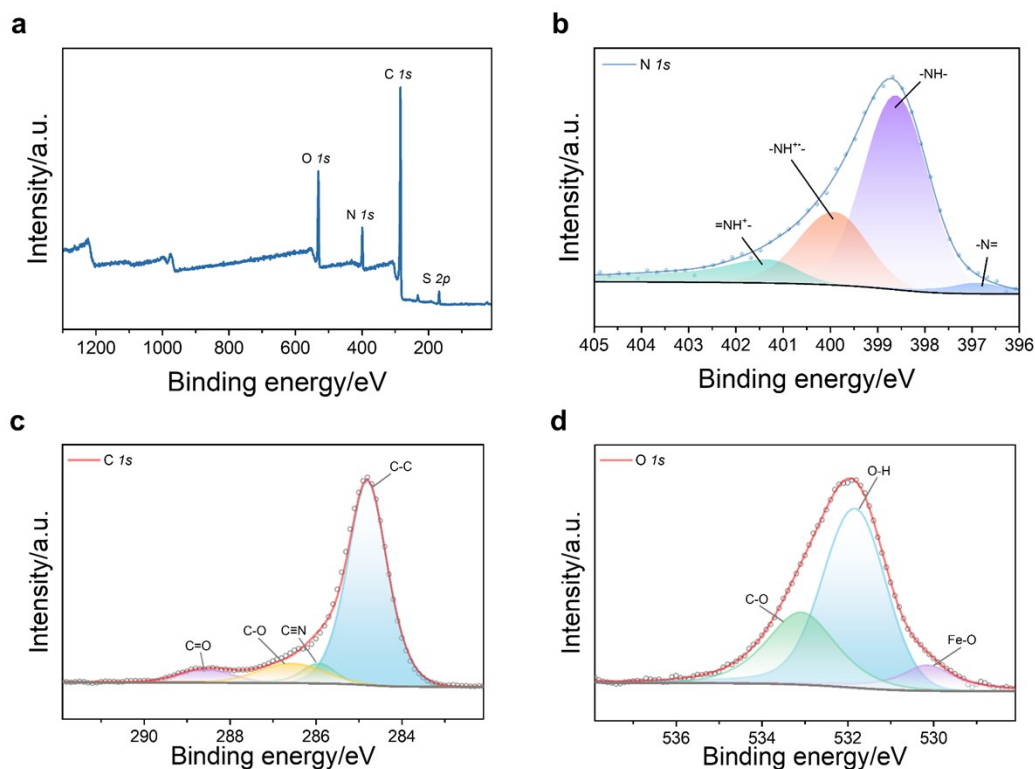


Figure S12. (a) XPS survey spectra and (b) N1s high-resolution spectra of PANI. (c) High-resolution C1s and (d) O1s spectra of PB-ECL.

Among these, the S2p peak originates from SO₄²⁻ anions, indicating successful doping with sulfuric acid during the electrodeposition process. The coexistence of =NH⁺, -NH⁺, -NH₂, and -N= confirms that the electrodeposited PANI-ECL is in a protonated semi-oxidized state, where chain growth proceeds synchronously with proton doping, albeit with a limited doping degree. The C-C, C-O, and C=O bonds at 284.8 eV, 286.6 eV, and 288.7 eV originate from incorporated impurities in the PB-ECL itself or from the testing environment, while the O1s peaks are primarily attributed to zeolitic water.

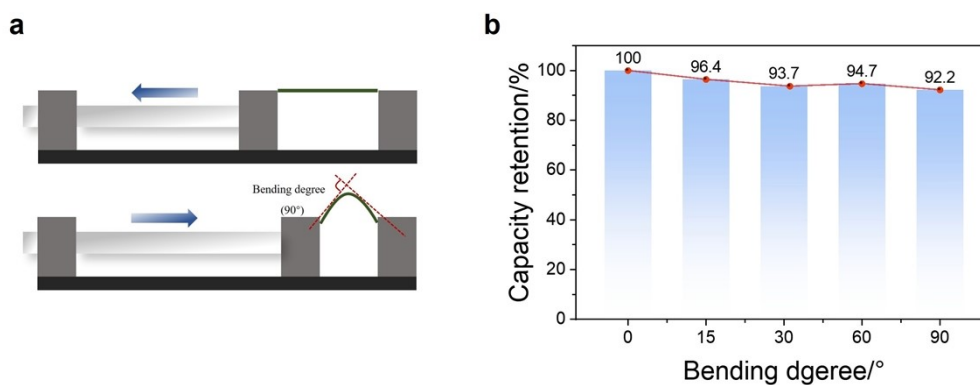


Figure S13. (a) Film flexural tester. (b) Capacity retention rate of the integrated PB-ECL/PANI-ISL structure that constitutes the Vis modulation region at different bending angles.

The D-ECF is constructed with PANI-ECL and PB-ECL as its surface electrochromic layers. Specifically, as established in our previous works^[6-8], the integrated PANI-ECL/PANI-ISL structure that constitutes the IR modulation region exhibits excellent matching and mechanical robustness. Furthermore, the bending resistance of the integrated PB-ECL/PANI-ISL structure that constitutes the Vis modulation region is evaluated using a film flexural tester (Fig. S13a) coupled with an electrochemical workstation. As shown in Fig. S13b, the integrated PB-ECL/PANI-ISL structure maintains over 92% capacitance retention within a 90° bending range, as determined by integrating the cyclic voltammetry curves, demonstrating that the synergistic compatibility between PB-ECL and PANI-ISL endows it with remarkable stability under complex deformations.

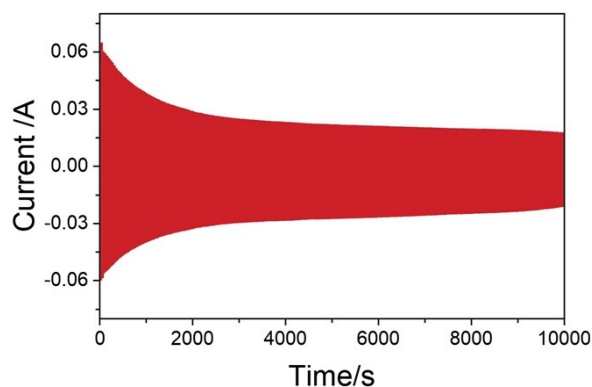


Figure S14. The current response of the Vis modulation region under multi-potential step (step 1:0.6 V and step 2: -0.8 V) cycling.

The cycling stability of the Vis modulation region with the integrated PB-ECL/PANI-ISL structure is found to be inferior to that of the integrated PANI-ECL/PANI-ISL structure in the IR modulation region, which has been extensively discussed in our previous work^[7,8]. This discrepancy can be primarily attributed to the intrinsic microstructural characteristics of the electrodeposited PB-ECL. Its rapid, non-equilibrium nucleation process during electrodeposition results in a denser morphology with higher defect density and greater internal stress. Such a structure is more susceptible to mechanical degradation (e.g., cracking and delamination) and accelerated Fe^{3+} dissolution during repeated ion insertion/extraction, ultimately leading to faster performance decay.

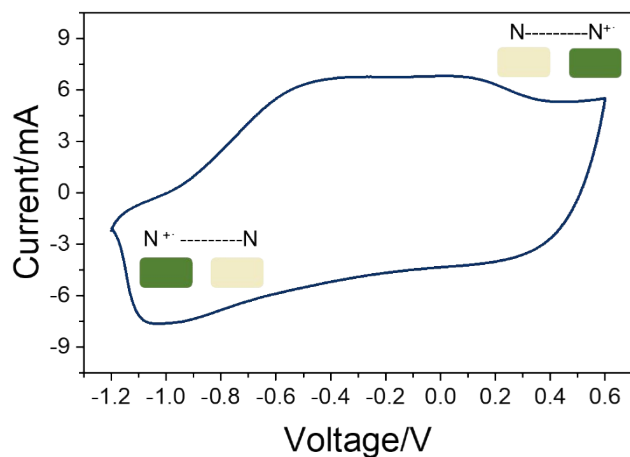


Figure S15. CV curves of the ECF with PANI-ECL symmetrically adapted to itself (PANI-ISL) under 15 mV S^{-1} .

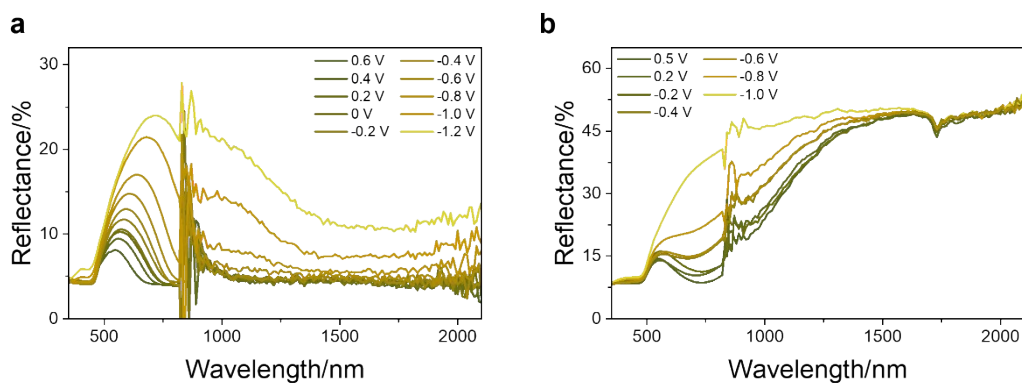


Figure S16. Vis-NIR reflectance spectra of (a) PANI-ECL and (b) PB-ECL.

Constrained by the fixed energy gap of PB, it cannot cover absorption in the NIR region beyond 800 nm. In contrast, the delocalization of conjugated chains induced by the polaron state formed via protonic acid doping in PANI enables broadband absorption that extends to the 800-2500 nm NIR region with tunability.

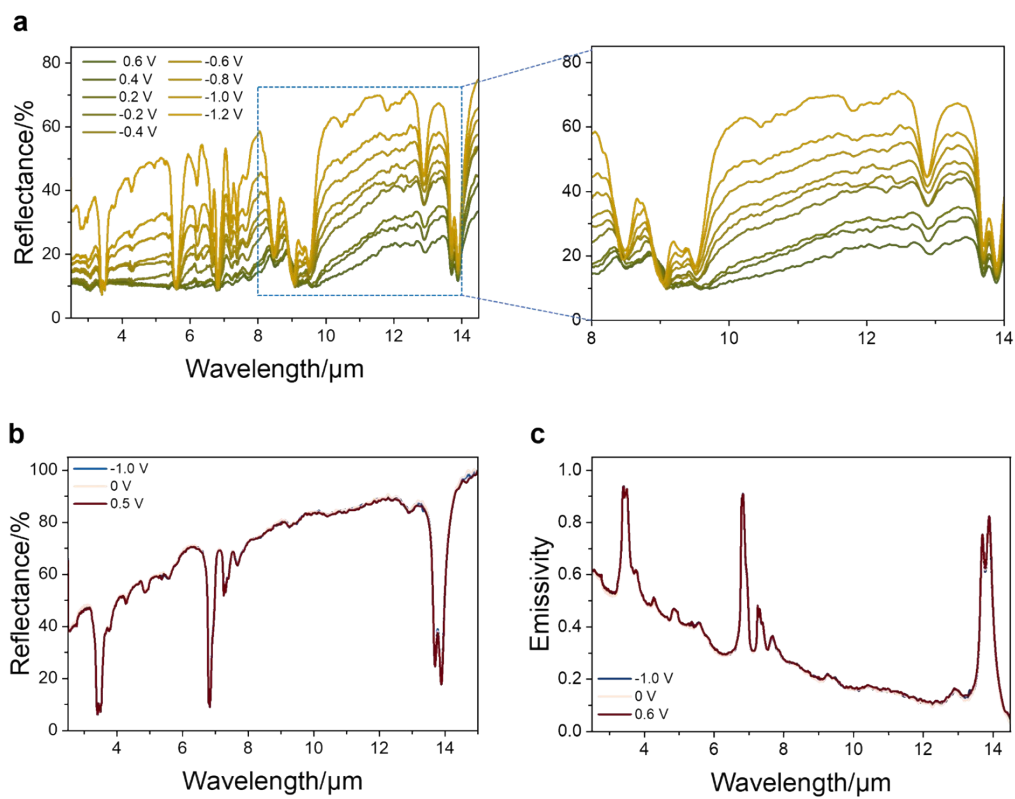


Figure S17. Mid-to-far IR reflectance spectra of (a) PANI-ECL and (b) PB-ECL. (c) Mid-to-far IR emissivity spectra of PB-ECL.

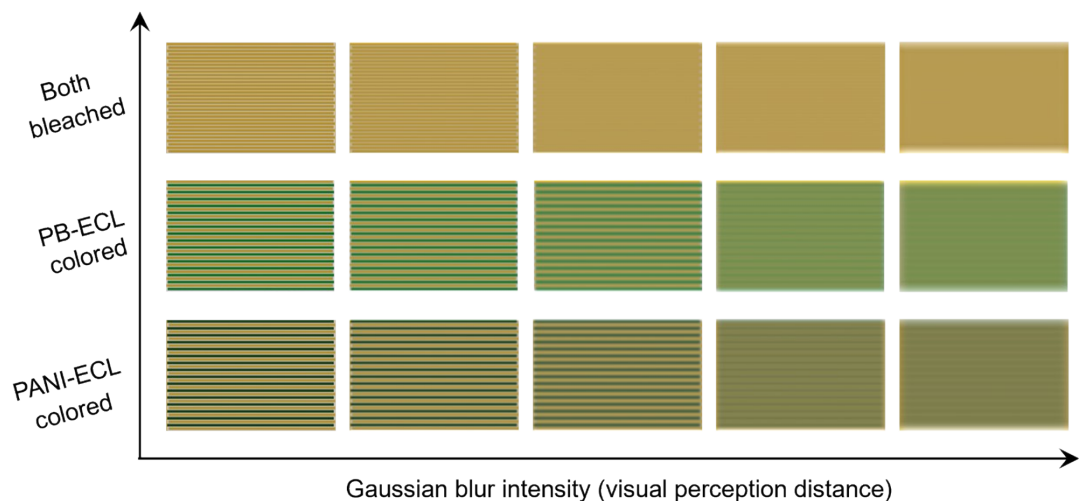


Figure S18. The standard deviation σ of the Gaussian function

$$G(x,y) = \frac{1}{2\pi\sigma^2} e^{-\frac{x^2+y^2}{2\sigma^2}}$$

governs the blurring degree. Herein, σ is proportional to the visual observation distance d , equivalent to detail compression in the image plane. Notably, when PB-ECL or PANI-ECL is colored individually, the interdigital stripes with significant color differences exhibit a "merged color" under increased blurring (i.e., increasing observation distance), effectively obscuring the surface details of the interdigital stripes. Although there exist matching and limitations between physiological mechanisms and mathematical approximations, Gaussian blurring can, to some extent, reflect the degradation of the human eye's ability to resolve details with increasing observation distance.

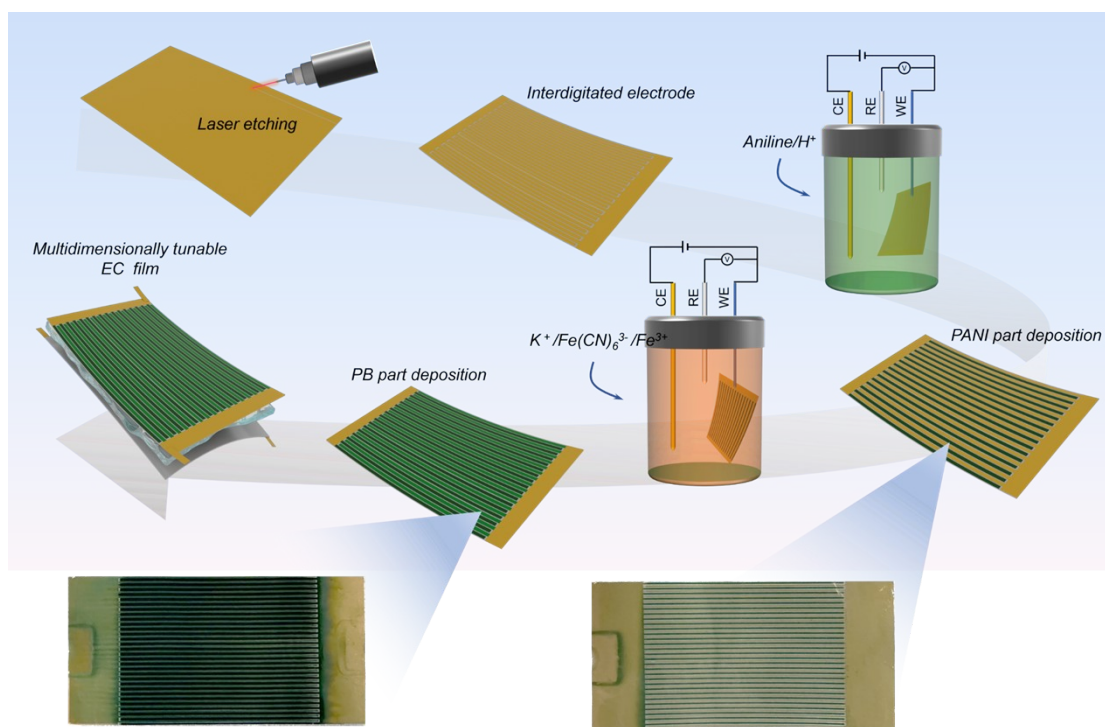


Figure S19. Fabrication of an interdigitated electrode and assembly process of D-ECF.

D-ECF is fabricated on flexible Au/Nylon 66 substrates, thus inherently compatible with flexible systems. Electron beam evaporation and laser etching technologies for preparing interdigitated electrodes exhibit high precision and mature technical application status, making them well-suited for large-area, continuous roll-to-roll large-scale industrial production.

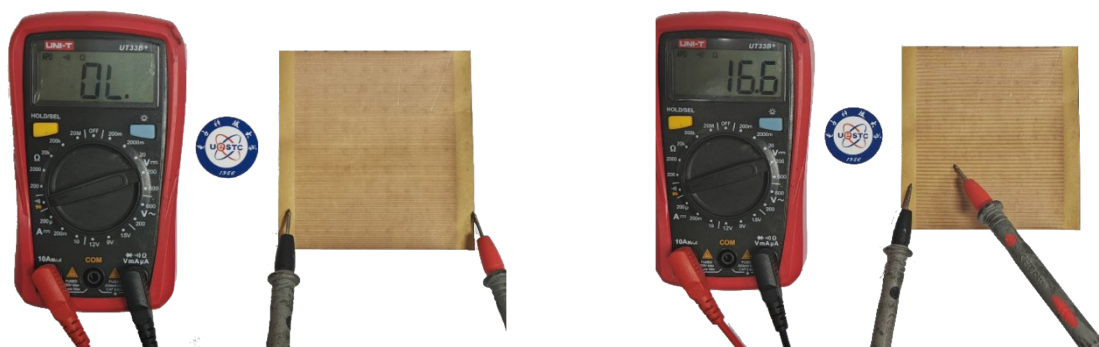


Figure S20. Conductivity of interdigitated electrode stripes.

The cost of D-ECF is significantly affected by the high price of Au in the Au/Nylon 66 substrates used. We plan to adopt an Ag+TiN composite in subsequent studies, which can ensure the electrical conductivity of the substrate while mimicking the golden visual characteristics of Au.

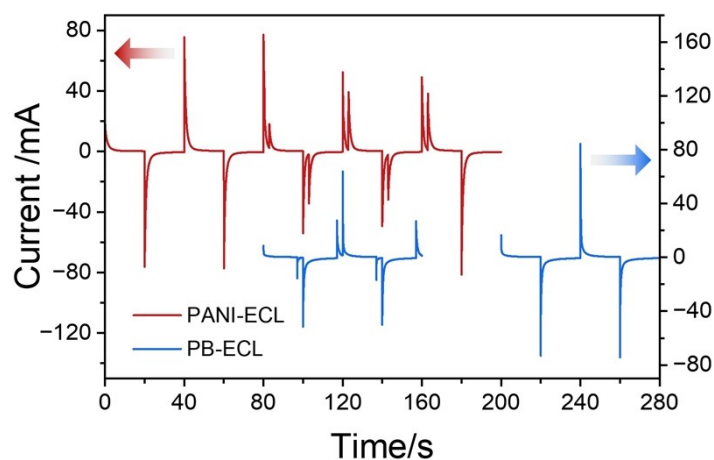


Figure S21. Current crosstalk arises from the simultaneous application of voltage to both the A-A' and B-B' electrode pairs.

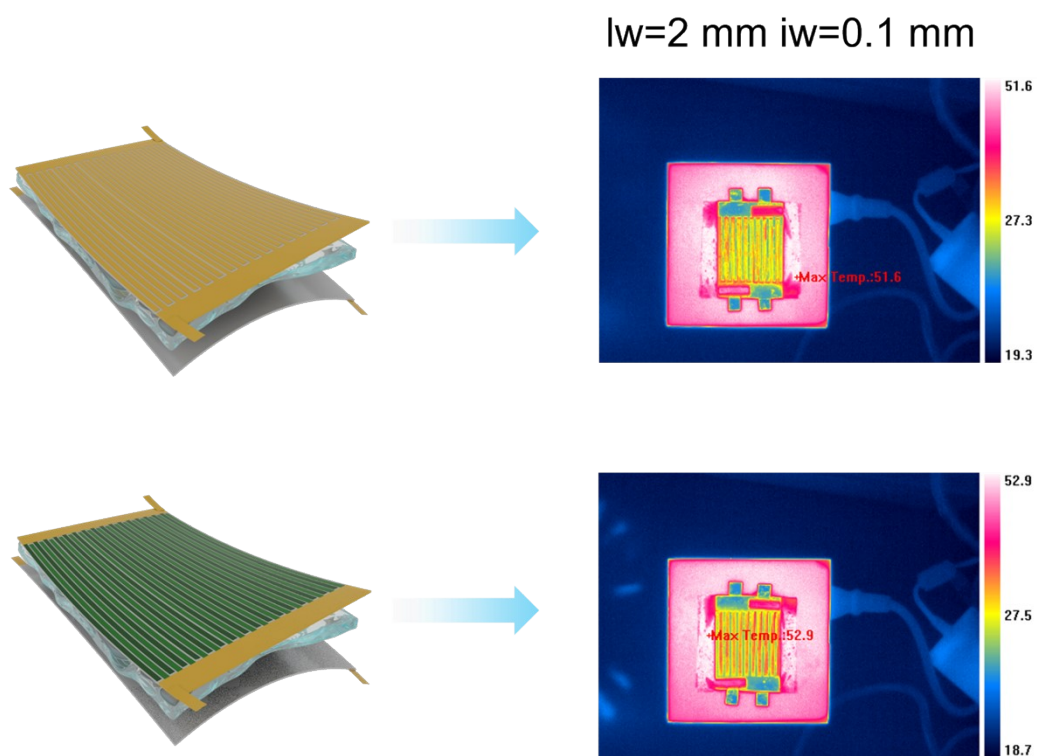


Figure S22. LWIR imaging of the D-ECF with $lw=2\text{ mm}$ and $iw=0.1\text{ mm}$ when both dual modulation regions are in colored and bleached states, respectively.

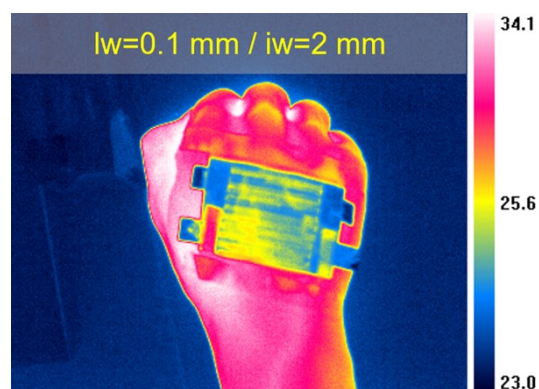


Figure S23. Thermal camouflage efficiency of D-ECF in LWIR imaging for $lw=0.1\text{ mm}$, $iw=2\text{ mm}$.

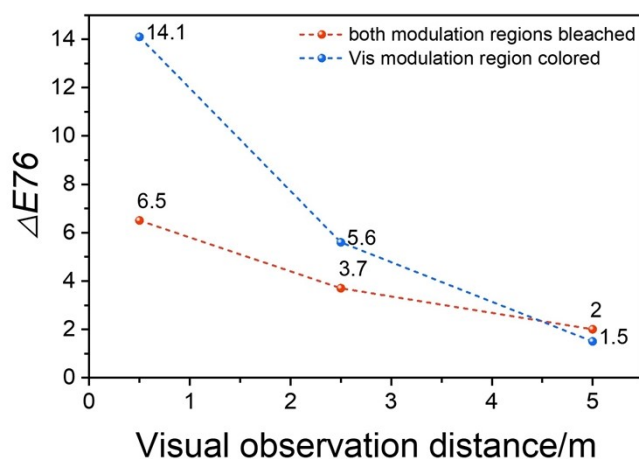


Figure S25. Variation in surface color difference $\Delta E76$ of adjacent interdigitated stripes for RD-ECF at different observation distances: Under the states of both Vis and IR modulation regions in bleached state or Vis modulation region in colored state.

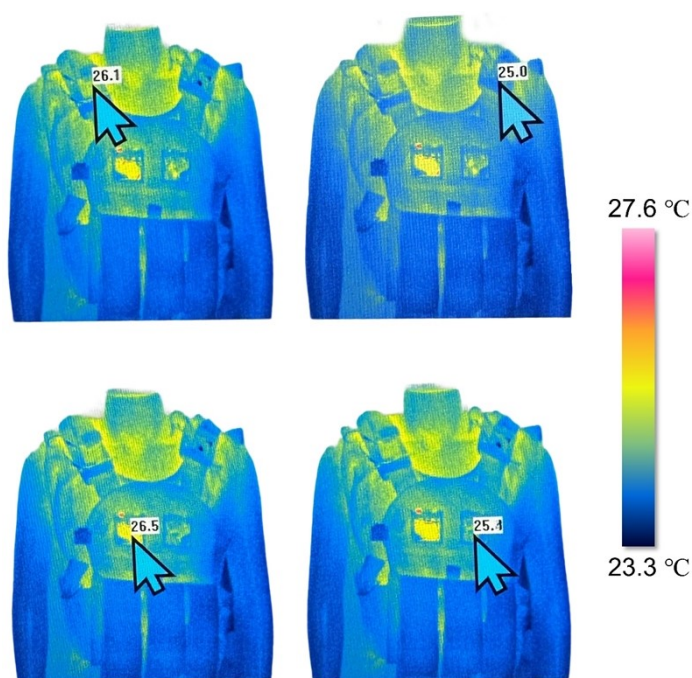


Figure S26. The imaging colormap is adjusted to a rainbow to more intuitively visualize the contrast in thermal infrared imaging among RD-ECF, LD-ECF, and PANI-ECFs. Specifically, the apparent temperatures of RD-ECF and bleached PANI-ECFs are higher than their true temperatures, which is attributed to strong environmental reflection caused by their low surface emissivity. In contrast, the apparent imaging temperatures of LD-ECF and colored PANI-ECFs are closer to their

true temperatures.

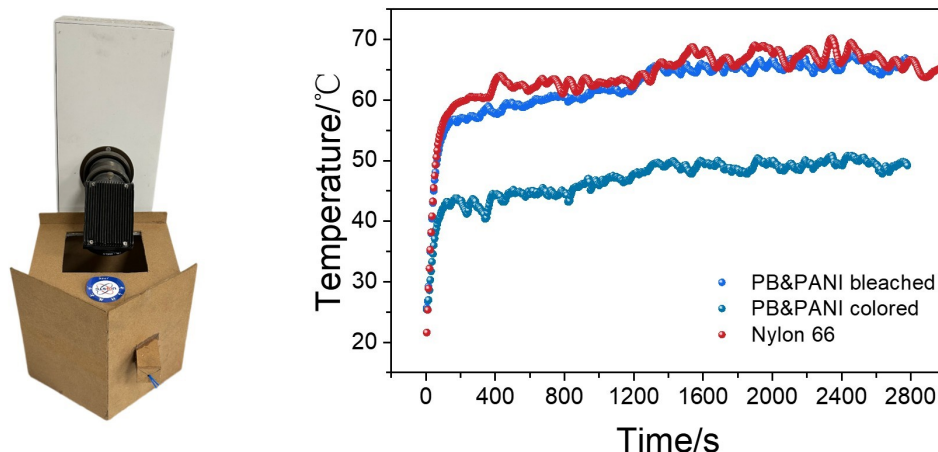


Figure S27. Experimental setup for simulated solar irradiation and the corresponding actual surface temperature evolution of the D-ECF.

At an ambient temperature of 20°C, the samples are exhibiting distinct heating behaviors due to their differing solar energy absorption capacities in the Vis spectrum, which constitutes the primary energy region of solar radiation. The white Nylon 66 substrate, serving as a control, is demonstrating the lowest absorption and thus showing the slowest rate of actual surface temperature increase. In contrast, when both the Vis and IR modulation regions of the D-ECF are in the colored state, its dark green appearance is resulting in strong solar energy absorption. Conversely, when both regions are bleached, the ECF is exhibiting the light-yellow color of the Au/Nylon 66 substrate, effectively reflecting solar energy and consequently minimizing absorption.

Table S1. Visual sensory colors and Vis reflectance spectra comparison of PB-ECL with different deposition times and PANI-ECL prepared by two-step potentiostatic cyclic electrodeposition for five cycles.


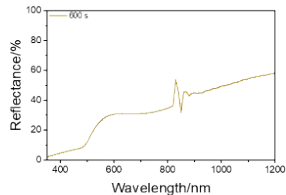

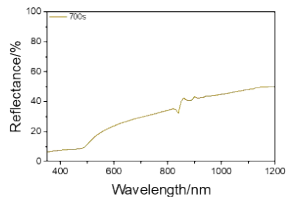

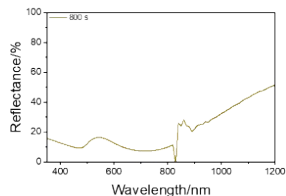

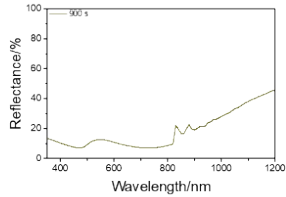
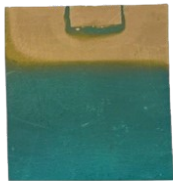
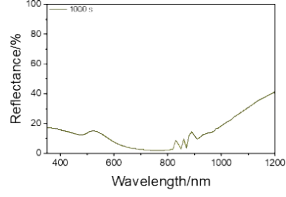

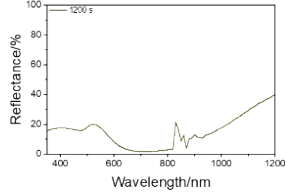
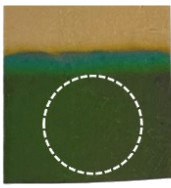
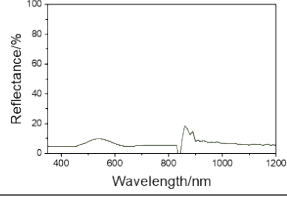
Preparation process	Digital photograph	Vis-NIR reflectance
-25 $\mu\text{A}/\text{cm}^2$ 600s		
-25 $\mu\text{A}/\text{cm}^2$ 700s		
-25 $\mu\text{A}/\text{cm}^2$ 800s		
-25 $\mu\text{A}/\text{cm}^2$ 900s		
-25 $\mu\text{A}/\text{cm}^2$ 1000s		
-25 $\mu\text{A}/\text{cm}^2$ 1200s		
Step1: 0.8V Step2: 0.6V Cycle 5		

Table S2. The fitted circuit diagram values and rel. std. error of the EIS curves of PB-ECL.

Index	fixed	parameter	start	end	rel.std.error(%)
1	0	R_s	3.030E+001	3.030E+001	2.023
2	0	C_{dl}	3.249E-007	3.249E-007	12.5
3	0	R_{ct}	1.111E+001	1.111E+001	5.215
4	0	Z_w	2.256E-003	2.256E-003	2.105

Measurement errors in impedance data = < 3.052 pct.

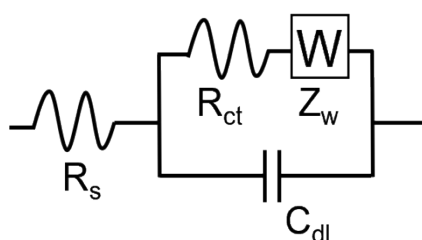


Table S3. The fitted circuit diagram values and rel. std. error of the EIS curves of PANI-ECL.

Index	fixed	parameter	start	end	rel.std.error(%)
1	0	R_s	3.529E+001	3.529E+001	0.784
2	0	C_{dl}	2.332E-005	2.332E-005	4.485
3	0	R_{ct}	1.419E+001	1.419E+001	1.911
4	0	Z_w	5.035E-002	5.035E-002	1.827
5	0	C_{ps}	2.512E-002	2.512E-002	0.915

Measurement errors in impedance data = < 1.071pct.

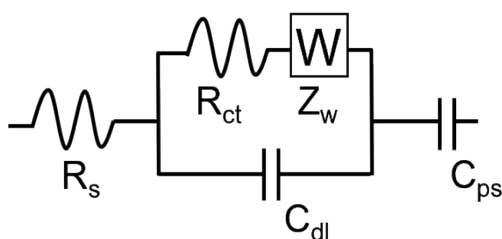





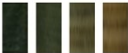


Table S4. Average emissivity (α - ϵ) of PANI-ECL at different voltages.

Voltage	3-5 μm	8-14 μm	2.5-15 μm
0.6 V	0.895	0.823	0.827
0.4 V	0.891	0.789	0.796
0.2 V	0.896	0.771	0.780
-0.2 V	0.877	0.702	0.719
-0.4 V	0.836	0.680	0.694
-0.6 V	0.826	0.650	0.668
-0.8 V	0.769	0.606	0.623
-1.0 V	0.721	0.563	0.579
-1.2 V	0.558	0.485	0.493

Table S5. Comparison of the performances of the D-ECF with literature.

Ref	Decoupled Mechanisms	Materials	Spectral range	Infrared emissivity regulation	Color	Color regulation
[1]	Fabry-Perot cavity	ITO/NiO/Ta ₂ O ₅ /Li/WO ₃ /ITO/Ge/HfO ₂	2.5–25 μm	2.5-25 μm =0.2		x
[2]	Fabry-Perot cavity	ITO/SiO ₂ /ITO/ITO/NiO/ZrO ₂ /Li/WO ₃ /ITO	2.5–25 μm	MWIR=0.42 LWIR=0.53		v
[3]	Fabry-Perot cavity	Al ₂ O ₃ /TiO ₂ /Ge/SiO ₂ /SiO/SiO/TiO ₂ /Ta ₂ O ₅ /Ge/Y ₂ O ₃ /MgO	8-16 μm	No regulation function		x
[4]	Electrochromic and Thermochromic	PB/Fe ₂ O ₃ /Si-SEBS/PANI	2.5-16 μm	2.5-16 μm =0.3/0.33/0.3		v
[5]	Photonic crystals and Electrochromic	PSNS/PE/MWCNT/IL/MWCNT/PE	7.5-13 μm	7.5-13 μm =0.47		x
This work	Electrochromic	PB/PANI	2.5-15.5 μm	MWIR=0.33 LWIR=0.34		v

Reference

- [1] W. Sun, X. Zhang, H. Zhang, Z. Ren, M. Chen, Y. Xiao, Z. Li, J. Deng, D. Yan, L. Zhang, Y. Li, *Laser Photonics Rev.*, 2023, **17**, 2300476.
- [2] H. Zhang, X. Zhang, W. Sun, M. Chen, Y. Xiao, Z. Ding, D. Yan, J. Deng, Z. Li, J. Zhao, Y. Li, *Adv. Funct. Mater.*, 2024, **34**, 2307356.
- [3] X. Ma, X. Teng, L. Xu, A. Bao, H. Qu, Q. Li, S. Zhang, J. Zhu, *Adv. Opt. Mater.*, **2025**, 2403438.
- [4] S. Song, T. Hao, B. Wang, D. Liu, Z. Ren, Y. Zhang, W. Liu, L. Zhang, Y. Li, *Adv. Opt. Mater.*, 2023, **11**, 2301065.
- [5] Y. Wang, L. Yuan, Y. Mao, C. Huang, J. Huang, X. Ma, Y. Qi, Y. Liu, H. Lin, X. Luo, *Nanophotonics*, 2024, **13**, 3123-3133.
- [6] C. Song, R. Zheng, Y. Li, M. Tian, W. Wu, Y. Tang, G. Zhou, J. Shao, *Rare Metals*, 2025, 44, 6102-6114.
- [7] H. Zhang, J. Yuan, Y. Liu, R. Zheng, C. Jia, *Electrochim Acta.*, 2025, 529, 146354.
- [8] Y. Liu, H. Zhang, S. Tang, R. Zheng, C. Jia, *J. Mater. Chem. A.*, 2024, 12, 32104-32116.